Chemical Science

ROYAL SOCIETY OF CHEMISTRY

EDGE ARTICLE

View Article Online
View Journal | View Issue

Cite this: *Chem. Sci.*, 2025, **16**, 18423

All publication charges for this article have been paid for by the Royal Society of Chemistry

Structural and spectroscopic basis of excitation energy transfer in microbial rhodopsins binding xanthophylls

Giacomo Salvadori, [a] Piermarco Saraceno, [b] Alisia Santomieri,[b] Chris John [b] and Laura Pedraza-González *[b]

Received 4th July 2025
Accepted 29th August 2025

DOI: 10.1039/d5sc04961j

rsc.li/chemical-science

Carotenoids serve as accessory light-harvesting pigments in microbial rhodopsins, but the mechanisms enabling efficient energy transfer in systems lacking canonical 4-keto groups remain poorly understood. Here, we combine long-timescale molecular dynamics, polarizable quantum mechanics/molecular mechanics (QM/MM) calculations, and excitonic modeling to elucidate the structural and electronic factors that govern carotenoid-to-retinal excitation energy transfer (EET) in the proton-pumping rhodopsin Kin4B8. Focusing on the xanthophylls, zeaxanthin and lutein, we show they support ultrafast (<100 fs) and high-efficiency (≈70%) EET, enabled not by specific functional groups but by precise protein–ligand geometry. The carotenoid's β-ring is anchored *via* a dynamic hydrogen-bonding network with Ser208 and Tyr209 within a conserved protein cavity, a configuration that optimally positions the retinal and carotenoid chromophores for strong excitonic coupling. Simulated absorption and circular dichroism (CD) spectra accurately reproduce observed spectral features, including the characteristic biphasic CD band shapes, notably the blue-shifted CD minimum compared to the absorption peak in the retinal region. A Förster-type kinetic model, built from QM/MM-derived parameters, recovers experimental transfer times and efficiencies. Our findings provide a mechanistic rationale for recent mutagenesis and carotenoid screening experiments, establishing that rhodopsin-based light harvesting is driven by protein-guided chromophore alignment rather than fixed carotenoid chemistry. This work establishes design principles for engineering photoactive proteins and offers a transferable framework for analyzing energy transfer across natural and synthetic light-harvesting systems.

1 Introduction

Light-harvesting in nature employs sophisticated molecular architectures to capture and channel solar energy with remarkable efficiency.[1] Among these systems, microbial rhodopsins have emerged as a particularly versatile family of photoreceptors, utilizing retinal chromophores to convert photons into diverse biological functions ranging from ion transport to sensory signaling.[2–6] While rhodopsins traditionally operate through direct excitation of their retinal chromophore, recent discoveries have revealed that some rhodopsin variants can expand their absorption spectrum by recruiting carotenoid molecules as antenna pigments.[5,7–20]

The mechanistic understanding of carotenoid-mediated light-harvesting in rhodopsins has undergone significant revision in recent years. Initial studies of the xanthorhodopsin-salinixanthin[7] complex and related systems established that 4-ketocarotenoids could function as efficient antenna pigments, transferring excitation energy to retinal.[7,9,13–15,21–23] The presence of the 4-keto group was proposed to be essential for this process, as it red-shifts the carotenoid absorption to achieve spectral overlap with retinal and facilitates favorable energy transfer. However, this mechanistic understanding was recently challenged by the discovery that rhodopsins can also form functional complexes with xanthophylls (*i.e.*, hydroxylated carotenoids) such as zeaxanthin, lutein, and nostoxanthin.[18,19,24–26] These carotenoids lack the 4-keto group entirely, yet still support efficient energy transfer to retinal with quantum yields of 40–55%. The initial discovery of this phenomenon was made by Chazan *et al.* (2023),[18] who showed that Kin4B8, a light-driven proton pump from an aquatic bacterium, binds zeaxanthin in a well-structured carotenoid channel and supports highly efficient energy transfer (Fig. 1a). Structural analysis through cryo-electron microscopy (PDB ID: 8I2Z[18]) revealed a unique binding architecture where the carotenoid's hydroxyl-bearing ring inserts into a specialized protein opening termed "fenestration". This fenestration, created by the small glycine residue at position 153, enables close chromophore–chromophore (*i.e.*, retinal-carotenoid)

[a]*Institute for Computational Biomedicine (INM-9), Forschungszentrum Jülich, 52428 Jülich, Germany*

[b]*Dipartimento di Chimica e Chimica Industriale, Università di Pisa, Via G. Moruzzi 13, 56124 Pisa, Italy. E-mail: laura.pedraza@unipi.it*

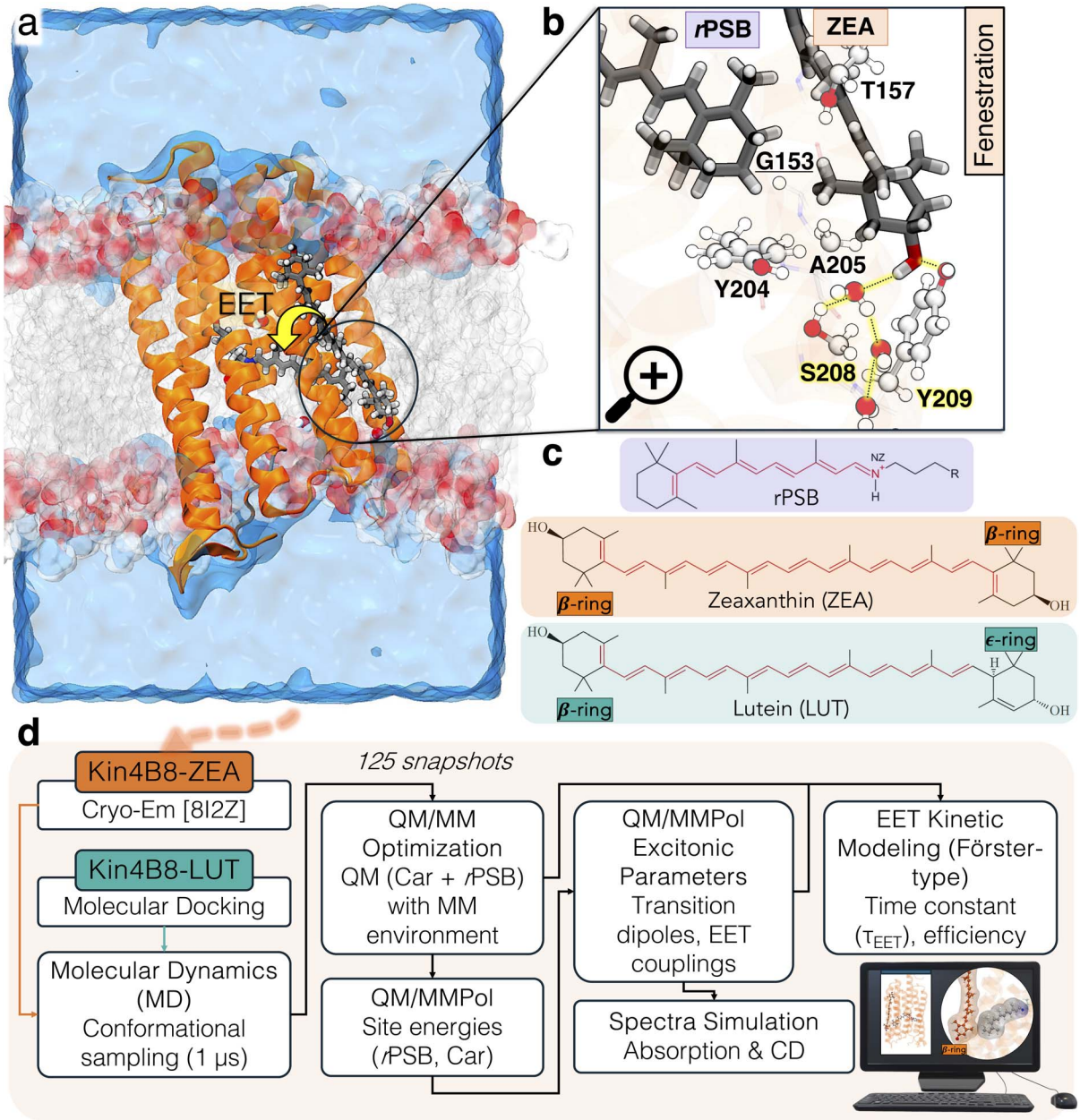

Fig. 1 Carotenoid binding and fenestration architecture in Kin4B8. (a) Overall structure of the Kin4B8-xanthorhodopsin complex embedded in a lipid bilayer, based on the cryo-EM structure (PDB ID: 8I2Z[18]). The protein is shown in cartoon representation, with the retinal chromophore (*r*PSB) and carotenoid depicted in gray licorice style. (b) Zoom-in view of the fenestration region, highlighting key residues involved in carotenoid binding: Gly153, Thr157, Tyr204, Ala205, Ser208, and Tyr209. The ZEA hydroxyl ring is positioned within the fenestration, forming interactions with surrounding residues. Dominant hydrogen bond interactions are indicated by dashed yellow lines. (c) Chemical structures of the *r*PSB, zeaxanthin (ZEA), and lutein (LUT), with the conjugated polyene region highlighted in red. (d) Multiscale computational protocol. All structural representations were generated using VMD (Visual Molecular Dynamics).[27]

interactions (Fig. 1b). Subsequent work by Das *et al.* (2025)[26] further elucidated the functional and structural basis for this interaction through mutational and spectroscopic analysis. They proposed that Ser208 and Tyr209 are critical for stabilizing the carotenoid *via* hydrogen bonding, and that mutation of Gly153 to phenylalanine (G153F) disrupts binding and abolishes excitation energy transfer (EET). A broad carotenoid screen revealed that chemical functionality alone does not predict energy transfer capability, highlighting the importance of protein-guided geometry and chromophore orientation.

Despite these structural insights, fundamental questions remain unanswered: what determines the binding specificity and orientation of different carotenoids? How do hydroxylated carotenoids achieve efficient energy transfer without 4-keto groups? What role does the protein environment play in

modulating electronic coupling? How do structural features translate into the observed spectroscopic signatures?

While recent experimental work has demonstrated the importance of carotenoid binding geometry and identified key residues required for chromophore anchoring, the underlying physical mechanisms, particularly the electronic and excitonic factors enabling ultrafast energy transfer, remain unresolved. Addressing these questions is essential for understanding the molecular evolution of light-harvesting systems and for engineering artificial photonic assemblies. In Kin4B8, xanthophyll binding has been shown to enhance proton-pumping activity,[18] consistent with an antenna function that boosts retinal excitation efficiency. This functional consequence underscores the biological relevance of efficient energy transfer and motivates a detailed understanding of the structural and electronic factors that enable it.

In this work, we employ a comprehensive multiscale computational approach to elucidate the structural and electronic factors governing excitation energy transfer in Kin4B8-xanthophyll complexes. Our methodology integrates microsecond-scale molecular dynamics (MD) simulations to capture dynamic protein-chromophore interactions, quantum mechanics/molecular mechanics (QM/MM) calculations with polarizable embedding to accurately compute electronic excitations, and excitonic modeling[28–31] to simulate spectroscopic observables and energy transfer dynamics (see Fig. 1d). Through this approach, we reveal how nature achieves efficient light-harvesting through precise structural complementarity rather than specific chemical functionalities, establishing design principles for biomimetic energy conversion systems.

2 Results and discussion

2.1 Selection of the protonation microstate

The photophysical properties of rhodopsins critically depend on the protonation states of residues surrounding the retinal protonated Schiff base (*r*PSB), particularly the counterion network.[2,32–40] In Kin4B8, two aspartate residues (Asp94 and Asp229, Fig. 2c) form the primary counterion system, but their protonation states could not be directly determined from the cryo-EM structure. To resolve this, we evaluated two plausible protonation microstates (pMS): pMS-1, with Asp94 protonated and Asp229 deprotonated, and pMS-2, with the reverse configuration (see Section S1, for full details). Each microstate underwent 1.0 μs MD simulations followed by QM/MM calculations. Structural analysis showed that pMS-1 better preserved the crystallographic water-mediated hydrogen bond between the *r*PSB nitrogen and Asp94 and yielded lower backbone RMSD values compared to pMS-2 (Fig. S1a). In contrast, pMS-2 formed a direct salt bridge and disrupted the Tyr61–Asp229 hydrogen bond observed in the cryo-EM structure, causing Tyr61 to reorient toward Asp94 (Fig. S1b–e). Spectroscopically, QM/MM calculations[35,41] on pMS-1 predicted an absorption maximum in better agreement with the experimental value of 549 nm[18] than pMS-2, which exhibited a significant red-shift. Based on both structural stability and spectroscopic agreement, summarized in Table S1, we selected pMS-1 (protonated Asp94, deprotonated Asp229) as the reference protonation microstate for all subsequent analyses.

2.2 Comparative analysis of zeaxanthin and lutein binding modes

Having established the protein's protonation state, we next investigated how zeaxanthin (ZEA) and lutein (LUT) interact with the Kin4B8 carotenoid-binding site. While ZEA's binding mode is resolved in the cryo-EM structure,[18] the orientation of LUT remains ambiguous due to its asymmetric β- and ε-rings (Fig. 1c). We evaluated two plausible LUT orientations *via* molecular docking and long-timescale MD simulations: one inserting the β-ring into the fenestration (pose A), and the other inserting the ε-ring (pose B) (Fig. S2a). Full simulation protocols are provided in Sections S3.1 and S3.2.

The fenestration is a narrow cavity shaped by both hydrophobic and polar residues, including Gly153, Thr157, Tyr204, Ala205, Ser208, and Tyr209 (Fig. 1b). While its architecture is largely hydrophobic, the presence of hydroxyl-containing side chains (Ser208 and Tyr209) enables specific water-mediated hydrogen bonding with the xanthophyll. Both ZEA and LUT in pose A formed a stable hydrogen-bond network involving these residues, effectively anchoring the hydroxylated β-ring within the cavity. In contrast, LUT pose B established weaker, transient hydrogen bonds, primarily with Ser208, and showed reduced stability.

These findings align with recent mutagenesis and QM/MM MD studies on ZEA,[26] which demonstrated that substitutions at Ser208 or Tyr209 disrupt binding and reduce EET efficiency in Kin4B8-ZEA. Their results also revealed dynamic cooperativity: weakening of one hydrogen bond coincided with strengthening of the other. Our microsecond MD simulations similarly showed flexible but persistent anchoring, reinforcing the functional role of this interaction network. While those studies focused exclusively on ZEA, our results demonstrate that the same anchoring mechanism extends to LUT, despite its asymmetric terminal rings, thereby providing a broader perspective on xanthophyll binding specificity in Kin4B8.

Enhanced sampling MD simulations further supported this picture: both ZEA and LUT pose A remained stably bound within the fenestration, while LUT pose B spontaneously dissociated. Simulations of the G153F mutant also resulted in complete carotenoid unbinding, consistent with the experimental observation that this mutation blocks binding and impairs energy transfer.[18]

Taken together, these findings support a conserved and cooperative anchoring mechanism in which both ZEA and LUT bind *via* their β-rings, stabilized by water-mediated hydrogen bonds with Ser208 and Tyr209. This structural arrangement preorganizes the xanthophylls within the protein cavity, facilitating efficient energy transfer. Accordingly, all subsequent spectroscopic and energy transfer analyses were performed using LUT pose A as the physiologically relevant binding mode. Further details on the structural and dynamical analyses are provided in Section S2.

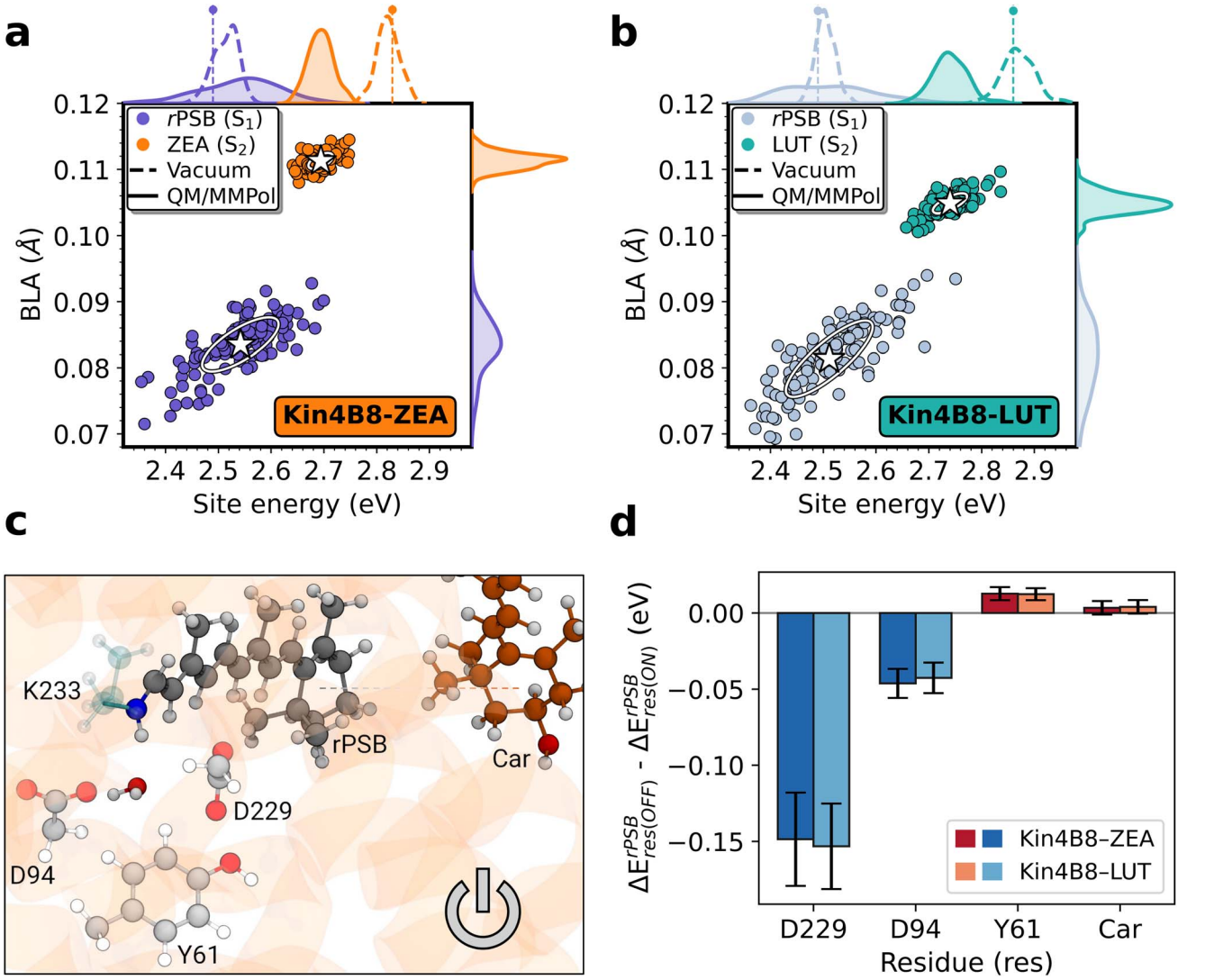

Fig. 2 Geometrical and color tuning analyses of *r*PSB in Kin4B8-Car complexes. (upper panel) Site energy *vs.* BLA for *r*PSB and Car in (a) Kin4B8-ZEA and (b) Kin4B8-LUT. Distributions in protein (solid) and vacuum (dashed) are shown alongside. White stars mark mean energies; ellipses represent 1σ covariance. Vertical dashed lines indicate vacuum site energies computed for gas-phase optimized geometries (*r*PSB: 2.49 eV, ZEA: 2.83 eV, LUT: 2.87 eV), providing reference values for comparison with the distributions. (c) The counterion environment surrounding the *r*PSB. Asp94 and Asp229, along with Tyr61, are shown as key residues forming the counterion triad. A water molecule mediating the interaction between the *r*PSB and Asp94 is indicated. (d) Average difference in *r*PSB excitation energy ($\Delta E^{rPSB}_{res(OFF)} - \Delta E^{rPSB}_{res(ON)}$ (eV)) upon electrostatic turn-off of selected residues and the carotenoid in ZEA and LUT systems. Error bars indicate standard deviation. Blue and red bars represent the blue- or red-shift effect, respectively. Data reported on $N = 110$ (ZEA) and $N = 116$ (LUT) structures. All structural representations were generated using VMD (Visual Molecular Dynamics).[27]

2.3 Excitonic model and spectra prediction

Based on the identification of the preferred binding modes of ZEA and LUT (pose A) within Kin4B8 using the pMS-1 model (Section 2.2), we examined the spectroscopic signatures arising from these specific chromophore arrangements and their interactions with the surrounding protein environment. To interpret the distinct features observed in the absorption and circular dichroism (CD) spectra of the Kin4B8-xanthorhodopsin complexes,[18] we simulated the spectra within the exciton framework.[31,42] Approximately 125 representative structures were extracted at 8 ns intervals from 1.0 μs MD trajectories and subsequently optimized using a QM/MM scheme, in which the QM region comprised the carotenoid-retinal dimer (Car-*r*PSB), treated at the density functional theory (DFT) level using the CAM-B3LYP[43]/6-31G(d)[44] functional and basis set combination (see Section S3.3). This choice is supported by extensive benchmark studies on systems containing either xanthophylls or *r*PSB, where CAM-B3LYP has consistently demonstrated superior accuracy in reproducing key structural features, such as bond length alternation (BLA), compared to other commonly used density functionals. The CAM-B3LYP/6-31G(d) level of theory has since been widely employed for structural and spectroscopic investigations of these chromophores, particularly in studies exploring environmental effects, including the

differences between vacuum conditions and protein embedding.[45–52] All QM/MM calculations in this study were run using a locally modified version of Gaussian.[53]

To calculate the spectra, we modeled the vibronic lineshape using spectral densities derived from normal mode analysis (see Section S4.2 for details). As a validation step, we first computed the absorption spectra of each chromophore, *r*PSB and the xanthophyll, individually. The resulting lineshapes reproduce the characteristic vibronic features of their respective bright states (Fig. S3), consistent with experimental observations and previous modeling studies.[54,55] This confirms the accuracy of our spectral density construction and supports their use in the excitonic simulations that follow. The theoretical approaches used to calculate optical lineshapes are described in Section S4.3.

2.3.1 Excitation energies and environmental effects. Vertical excitation energies were computed using time-dependent DFT (TD-DFT)[56] at the CAM-B3LYP[43]/6-31+G(d) level within a polarizable embedding QM/MM(Pol) framework,[29,57–63] applied to the optimized geometries (see Section S3.3). These site energies correspond to the $S_0 \rightarrow S_1$ transition for *r*PSB and the $S_0 \rightarrow S_2$ transition for the carotenoids.

In the protein environment, the *r*PSB site energies span a broad range (2.3–2.8 eV, mean ~2.5 eV; Fig. 2a and b), reflecting substantial variations in the electrostatic environment sampled during 1.0 μs MD simulations. In contrast, Car site energies are more narrowly distributed (2.62–2.74 eV for ZEA; 2.66–2.86 eV for LUT), indicating greater robustness to environmental variation. The slightly higher average site energy for LUT (2.76 eV) relative to ZEA (2.68 eV) is consistent with the experimentally observed blue-shift in Kin4B8-Car absorption.[18,26]

To disentangle the contributions of chromophore geometry and environment to excitation energy variation, we computed vacuum excitation energies for both *r*PSB and Car using the same geometries sampled from the protein-embedded QM/MM optimizations. As shown in Fig. 2a and b, the site energy distribution for *r*PSB narrows substantially in the absence of the protein matrix (mean: 2.51 eV), whereas the Car distributions retain a similar width but exhibit a noticeable blue-shift relative to their corresponding protein-embedded values (mean: ZEA = 2.82 eV, LUT = 2.87 eV). Notably, these vacuum distributions fall within the same energy range as the site energies computed for gas-phase optimized geometries (*r*PSB: 2.49 eV, ZEA: 2.83 eV, LUT: 2.87 eV), highlighting their consistency with fully relaxed reference structures. Moreover, the ZEA vacuum mean aligns well with a previously reported value of 2.89 eV, obtained from gas-phase geometry optimization and vertical excitation energy calculations at the TD-CAM-B3LYP/6-31G(d) level,[49] further supporting the reliability of our approach. Taken together, these results confirm that the broad energy variation observed for *r*PSB arises primarily from electrostatic interactions, not from structural distortions alone.

BLA is a meaningful structural descriptor of intrinsic electronic tuning in conjugated systems.[64,65] It is defined as the average difference between the lengths of alternating single and double carbon–carbon bonds along the conjugated π-system (eqn (1)):

$$\mathrm{BLA} = \frac{1}{N_s}\sum_{i=1}^{N_s} d_s^{(i)} - \frac{1}{N_d}\sum_{i=1}^{N_d} d_d^{(i)} \quad (1)$$

Here, N_s and N_d denote the number of single and double bonds, respectively, while $d_s^{(i)}$ and $d_d^{(i)}$ represent the length of the *i*-th single and double bond. A lower BLA value typically indicates increased electronic delocalization, which in turn affects the excitation energy and optical properties of the chromophore.

In this study, the BLA parameter encompasses both the polyene backbone and the conjugated ring(s) of the studied chromophores (*i.e.*, *r*PSB, ZEA, LUT), with the relevant bonds highlighted in red in Fig. 1c. For both chromophores, we observe a positive correlation between BLA and excitation energy, where higher BLA values (*i.e.*, more localized π-electron density) lead to blue-shifted transitions.[48] This correlation holds both in vacuum and in the protein, but for *r*PSB, environmental electrostatics significantly modulate the absolute site energies and amplify the overall spread (Fig. 2a and b).

To further analyze environmental contributions to *r*PSB spectral tuning, we performed a color-tuning[66] analysis, by selectively turning off electrostatic interactions (*i.e.*, MM point charges and polarizabilities) from key residues near the *r*PSB (Asp94, Asp229, Tyr61) and the carotenoid itself, following a well-established QM/MM strategy[67] widely employed in rhodopsin proteins.[33,34,36,68–74] As shown in Fig. 2d, Asp229 (deprotonated) emerged as the dominant electrostatic modulator of *r*PSB excitation energy, followed by Asp94 (protonated), while Tyr61 had minimal influence. The carotenoid had a negligible effect on *r*PSB site energy in both ZEA- and LUT-bound systems, consistent with their similar absorption maxima.[18] Further analysis is provided in Section S1.2 (Fig. S4).

Together, these results reveal that while intrinsic geometric fluctuations (*e.g.*, BLA) contribute to excitation energy tuning, the dominant source of spectral heterogeneity in *r*PSB is the local electrostatic environment, particularly due to the charged counterion pair. This explains the subtle shift in *r*PSB absorption to carotenoid identity, and highlights Asp229 and Asp94 as key determinants of spectral tuning in Kin4B8.

We next examined the transition electric dipole moments (μ) associated with the computed site energies. As shown in Fig. 3a and b, red-shifted *r*PSB geometries, typically characterized by lower BLA, exhibit larger transition dipoles, and are more prevalent during the first 500 ns of simulation. This suggests that a protein-induced rearrangement at later timescales reduces conjugation, thereby weakening the $S_0 \rightarrow S_1$ transition dipole. The average value of |μ| for *r*PSB is approximately 9.5 D in both complexes, consistent with reported values for bacteriorhodopsin (10.7 D)[47] and the xanthorhodopsin–salinixanthin complex (11.9 D),[75] a light-harvesting proton pump found in the extremely halophilic eubacterium *Salinibacter ruber*.[76]

For the carotenoids (Fig. 3c and d), ZEA shows a narrow distribution of |μ| centered at 12.4 D. In contrast, LUT exhibits a bimodal distribution, with peaks at approximately 11.5 D and 12.3 D. This variation arises from conformational flexibility of

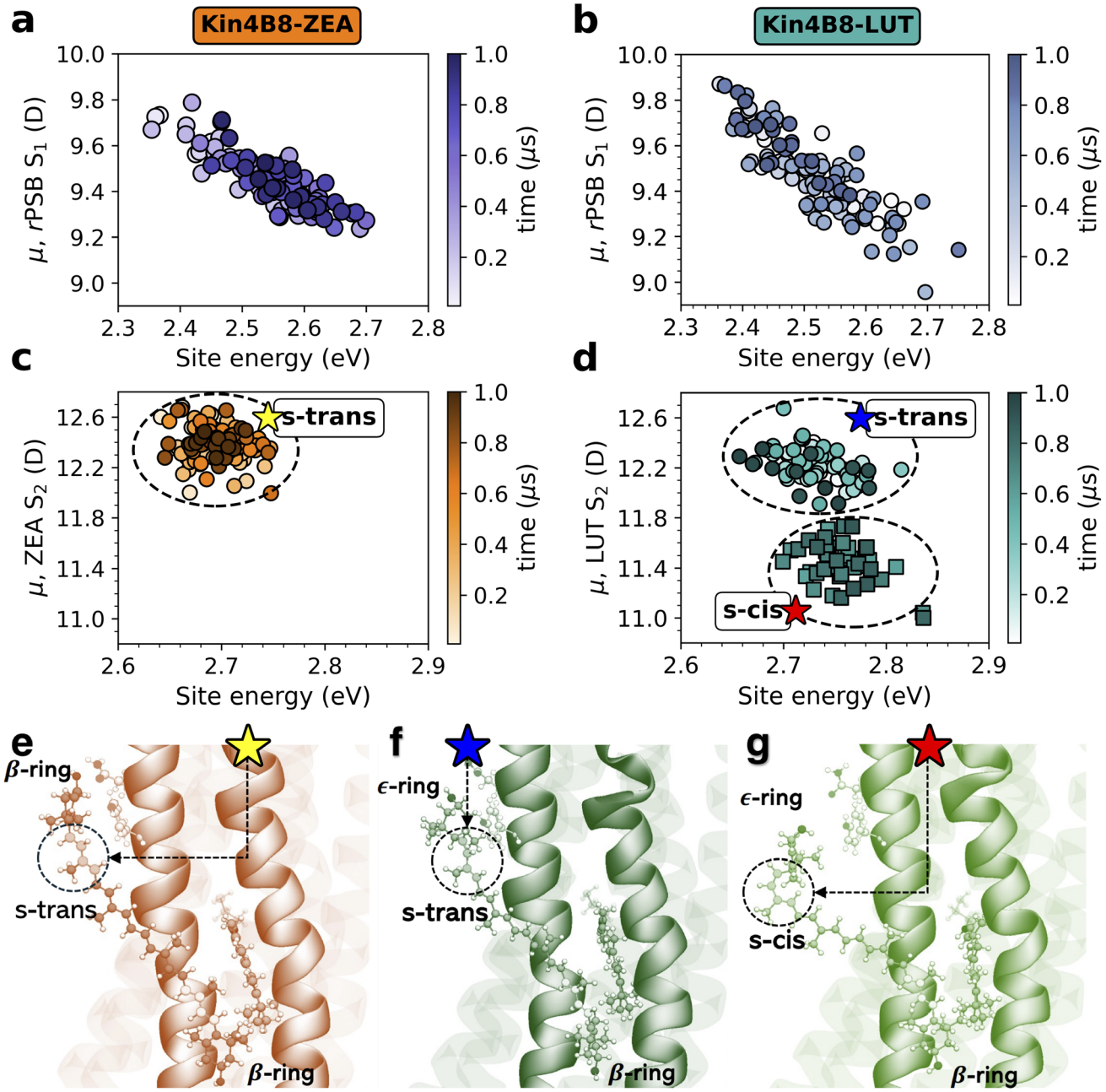

Fig. 3 Correlation between transition electric dipole moment (μ) and site energy for retinal protonated Schiff base (*r*PSB) and carotenoid (Car) sites in the Kin4B8-Car complexes. Panels (a) and (b) show data for *r*PSB in Kin4B8-ZEA and Kin4B8-LUT, respectively. Panels (c) and (d) depict the same analysis for ZEA and LUT. In (c) and (d), s-trans and s-cis conformations of the carotenoids are highlighted with dashed circles, illustrating their clustering according to dipole strength. Panels (e), (f), and (g) display representative structures of ZEA in the s-trans conformation in Kin4B8-ZEA, and LUT in the s-*trans* and s-*cis* conformations in Kin4B8-LUT, respectively.

LUT, particularly the single-bond dihedral in the ε-ring terminal (Fig. 3f–g). Structures with larger |μ| values adopt an s-*trans* conformation (similar to ZEA, Fig. 3e), while smaller |μ| values correspond to an s-*cis* geometry that introduces distortion. As shown in Fig. 3d, LUT switches between these conformers over the simulation, adopting the s-*cis* form around 500 ns and returning to s-*trans* near 800 ns. These transitions highlight LUT's conformational flexibility and its impact on electronic transition properties.

2.3.2 Electronic coupling of EET. To assess excitation energy transfer parameters, we computed electronic couplings between the Car(S_2) and *r*PSB(S_1) states. Since the associated transitions are bright singlet excitations, the coupling was evaluated from the coulomb interaction between their transition densities (eqn (S1)), obtained from TD-DFT calculations within a polarizable embedding QM/MMPol framework (eqn (S2))[29–31,42] (see Section S3.3 for details).

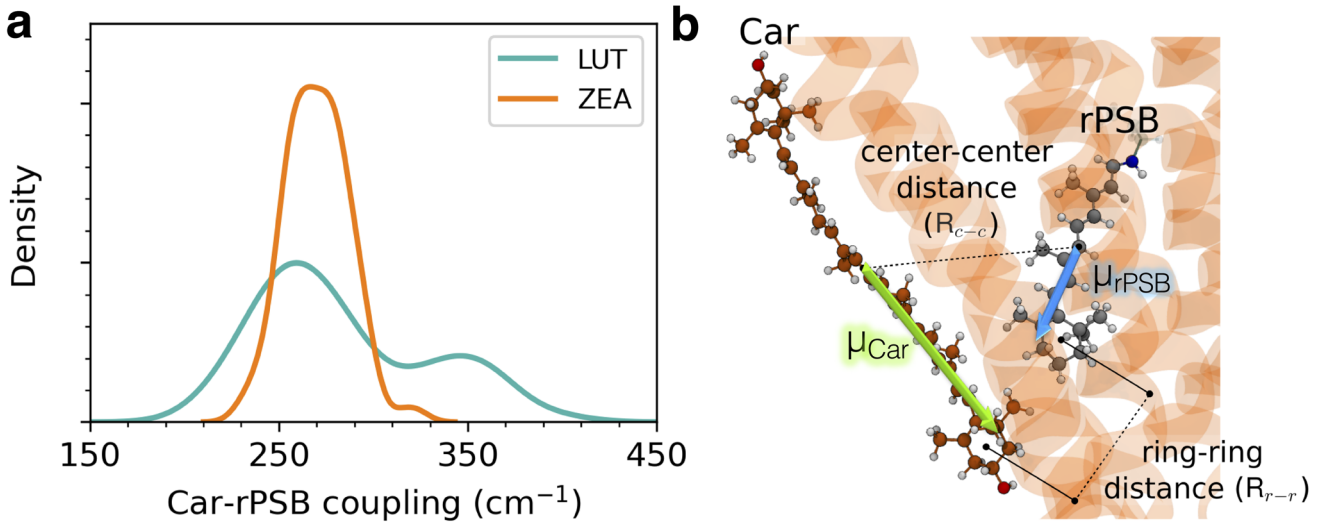

Fig. 4 Electronic couplings between carotenoid and retinal. (a) Distributions of ZEA-*r*PSB and LUT-*r*PSB couplings. (b) Illustration of the zeaxanthin-retinal dimer in the Kin4B8-ZEA complex; we explicitly show the quantities mainly affecting the electronic coupling, which are the center–center distance (R_{c-c}), and the ring–ring distance (R_{r-r}). The electric transition dipole moments (μ) are also depicted as green and blue arrows for ZEA (μ_{Car}) and *r*PSB (μ_{rPSB}), respectively.

As shown in Fig. 4a, the Kin4B8-ZEA complex exhibits a narrow coupling distribution centered around 270 cm^{-1}. In contrast, the Kin4B8-LUT (pose A) complex displays a broader, bimodal distribution, with peaks at *ca.* 250 cm^{-1} and 350 cm^{-1}, and a mean coupling of 284 cm^{-1}. These values fall within the expected range for efficient EET in carotenoid(S_2)-retinal(S_1) and carotenoid(S_2)-chlorophyll systems, where coupling strengths of 150–350 cm^{-1} have been reported.[7,77,78]

To understand these coupling patterns, we examined chromophore geometries, illustrated in Fig. 4b. The average distance between the center of mass of the chromophores (R_{c-c}) is 12.49 ± 0.13 Å for ZEA and 12.28 ± 0.21 Å for LUT (Fig. S5b). The average center-to-center distance between the β-ionone ring of *r*PSB and the fenestrated carotenoid ring (R_{r-r}) are shorter: 7.53 ± 0.04 Å (ZEA) and 7.11 ± 0.10 Å (LUT), consistent with close contact and strong coupling. We also analyzed transition dipole orientations, which supported a geometry conducive to efficient energy transfer. These geometrical parameters are consistent with previous studies on xanthorhodopsin, which showed that EET efficiency depends strongly on the spatial arrangement of the donor and acceptor chromophores.[7–9,76,79]

Next, we analyzed how geometric fluctuations of the chromophores relate to excitonic coupling. In Kin4B8-LUT, the inter-ring distance R_{r-r} varies between 6.0 and 8.5 Å, with a clear correlation to coupling strength. Kin4B8-ZEA shows a narrower R_{r-r} range (7.0–8.0 Å), associated with reduced coupling variability (Fig. S5a). In contrast, the center-to-center distance R_{c-c} exhibits weaker correlation with coupling in both complexes (Fig. S5b). Notably, conformational changes like s-*cis* to s-*trans* isomerization can alter R_{c-c} significantly while leaving R_{r-r} largely unaffected (see Fig. 3).

These results underscore R_{r-r} as a more reliable structural descriptor of coupling in this rhodopsin system, especially under conditions where the dipole–dipole approximation breaks down due to short intermolecular distances or distorted geometries.[29,77,79]

Finally, the computed couplings agree well with experimental estimates for the xanthorhodopsin–salinixanthin complex (160–210 cm^{-1}),[9] supporting the accuracy of the QM/MMPol method and confirming that the Kin4B8 complexes operate within an effective EET regime.

2.3.3 Absorption and circular dichroism spectra. In Fig. 5, we present simulated absorption and CD spectra for Kin4B8-ZEA and Kin4B8-LUT complexes, alongside experimental data reported by Chazan *et al.*[18] All spectra shown in this article have been computed with the Python3-based pyQME software package,[80,81] developed in our group.

To interpret the origin of the main absorption bands, we analyzed the individual contributions from *r*PSB and the carotenoid chromophores (see Fig. S6–S9, panel a). From this decomposition, we assigned the 300–480 nm region primarily to the carotenoid S_2 transition, while the broader 500–700 nm band arises from the *r*PSB S_1 transition. The *r*PSB band shows an absorption maximum near 549 nm.

To reproduce the position of the retinal band, we applied a site-energy shift of +0.2 eV (Fig. S10a). This value is notably smaller than the +0.4 eV shift reported in a previous study that employed a similar computational methodology for site energy prediction in other microbial rhodopsins.[63] In that work, proteins were modeled in the gas phase with limited conformational sampling restricted to 10 nearly identical structures. We attribute the reduced shift observed in our case to three key factors: (i) a more realistic model of the membrane-embedded protein–carotenoid complex, (ii) significantly broader conformational sampling (≈125 structurally diverse snapshots) derived from long-timescale MD simulations, and (iii) the inclusion of vibronic reorganization effects.

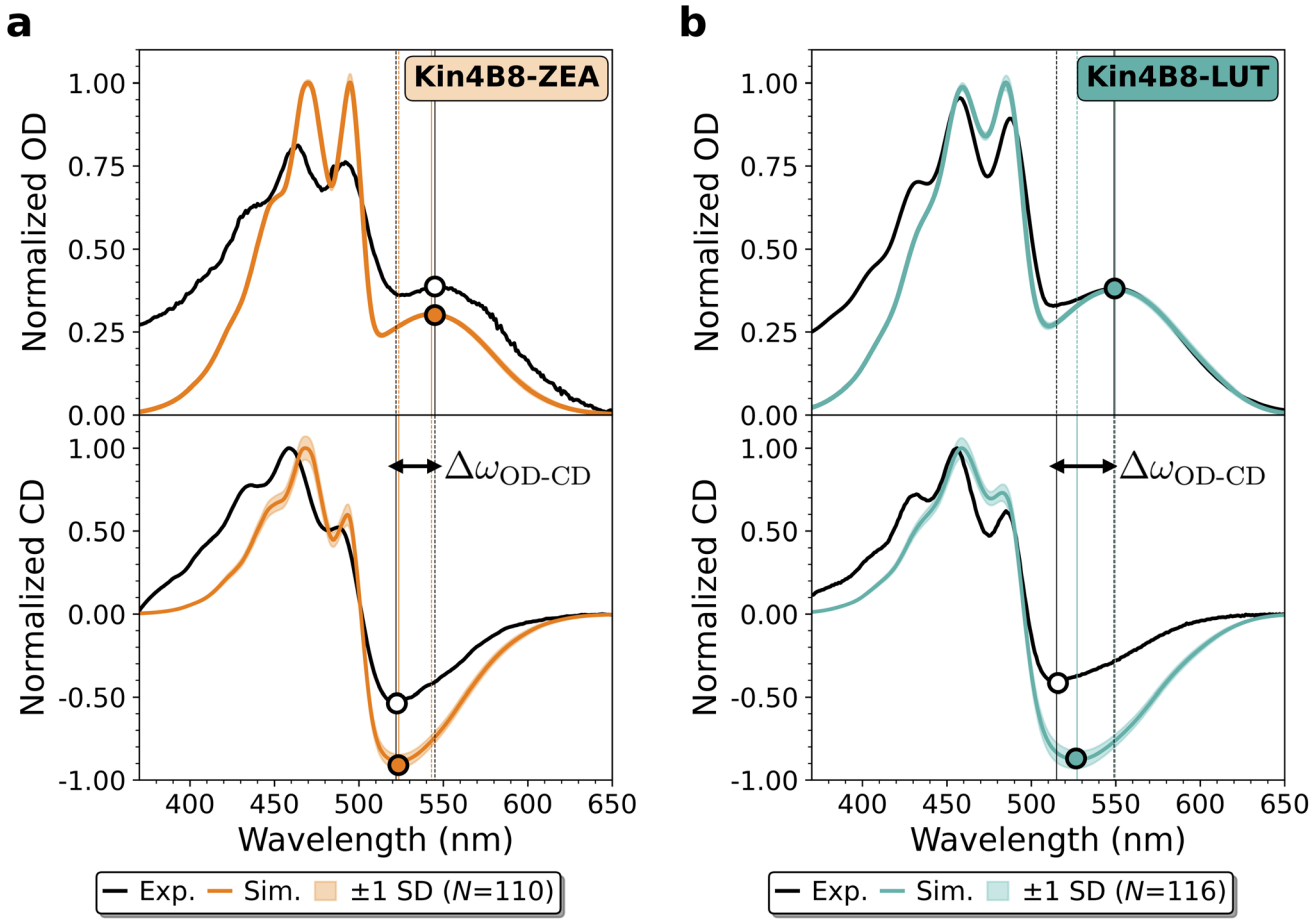

Fig. 5 Simulated absorption and circular dichroism spectra of the (a) Kin4B8-ZEA and (b) Kin4B8-LUT complexes. Each spectrum represents the ensemble average of $N = 110$ (ZEA) and $N = 116$ (LUT) replicas and is normalized to its respective mean maximum intensity. Shaded regions indicate the standard deviation estimated *via* bootstrapping over 1500 resampled ensembles. Absorption maxima and CD minima in the *r*PSB region are indicated by circles, as well as by vertical dashed and solid lines, respectively. Experimental spectra are adapted with permission from ref. 18.

Having established the origin and spectral positioning of the absorption bands, we next turned to the circular dichroism (CD) spectra to gain additional insight into the spatial arrangement and interactions between the chromophores. In the absence of a bound carotenoid, Kin4B8 exhibits a weak positive CD signal centered at the retinal absorption band, which reflects the intrinsic CD of *r*PSB.[18] Upon carotenoid (*i.e.*, ZEA and LUT) binding, a biphasic CD profile is observed: a negative band in the *r*PSB region and a positive one in the carotenoid region, with the *r*PSB minimum blue-shifted by ~20 nm with respect to absorption maximum. Similar shapes have been reported in other carotenoid-binding rhodopsins.[19,24,26,75,82]

To further interpret this CD profile, we analyzed its intrinsic and excitonic components.[42] In Kin4B8-LUT pose A, where the β-ionone ring occupies the fenestrated site, we found a positive CD signal of the carotenoid's intrinsic component, mirroring Kin4B8-ZEA (see Fig. S6b and S8b). In contrast, pose B (ε-ring in the fenestration) showed a negative carotenoid CD signal (Fig. S9b). These results support pose A as the preferred binding mode for LUT, given its positive carotenoid CD contribution that mirrors the behavior observed for ZEA. For both complexes, we found that the *r*PSB CD contribution remained negative, in agreement with prior studies,[75] and this consistent baseline helps isolate the spectral changes arising from excitonic coupling.

To assess the impact of excitonic coupling, we varied the Car(S_2)-*r*PSB(S_1) coupling strength (V_{C-R}) from 0 to 400 cm^{-1}, as shown in Fig. S10. The absorption spectrum showed only a slight red-shift (~10 nm) in the *r*PSB region, consistent with weak exciton splitting due to the large energy gap between *r*PSB and Car. In contrast, we observed a much stronger response in the CD spectra (see Fig. S10b). Specifically, as the coupling strength increased, the CD minimum became increasingly blue-shifted relative to the *r*PSB absorption maximum. We denote this offset as $\Delta\omega_{\text{OD-CD}}$ (see Fig. 5). Interestingly, even in the absence of coupling, our simulations reproduce the correct sign of the CD bands. This stands in contrast to previous modeling of the xanthorhodopsin–salinixanthin system, where decoupled chromophores still produced a biphasic CD signal, but with both bands showing signs opposite to the experimental ones.[75] Such disagreement is expected, as the intrinsic contributions have much lower intensity than the excitonic ones. As the

coupling strength increases, both the total CD signal and the spectral offset between the *r*PSB absorption maximum and the CD minimum ($\Delta\omega_{OD-CD}$) increase, leading to improved agreement with experiment.

Strikingly, our simulations suggest that the spectral offset $\Delta\omega_{OD-CD}$ correlates with EET efficiency, a trend that is qualitatively supported by recent experimental data on several Kin4B8-carotenoid complexes.[26] Specifically, astaxanthin and canthaxanthin, both of which bind to Kin4B8 but exhibit low energy transfer efficiencies (18% and 9%, respectively), display CD minima that coincide with the *r*PSB absorption maximum. In contrast, nostoxanthin, which supports a significantly higher EET efficiency of ~40%, shows a CD minimum blue-shifted by approximately 25 nm relative to the absorption peak, similar to the behavior observed for zeaxanthin and lutein.[18] Although the dataset is limited, this pattern suggests that $\Delta\omega_{OD-CD}$ may serve as an indirect spectroscopic indicator of the excitonic coupling strength between carotenoid and retinal, and by extension, of EET functional efficiency in rhodopsin-carotenoid systems.

These findings collectively indicate that, while excitonic interactions are not the sole determinant of the CD band sign, they are essential for accurately reproducing both the magnitude and spectral positioning of CD signals in Kin4B8. Furthermore, $\Delta\omega_{OD-CD}$ emerges as a potentially valuable experimental marker of excitonic coupling strength and photofunctional relevance in rhodopsin-carotenoid systems.

2.4 Excitation energy transfer

We conclude our analysis by examining the mechanism of excitation energy transfer from the carotenoid to retinal in the Kin4B8 complexes. This final section builds on the previous characterization of site energies, transition dipole properties, and excitonic couplings (Section S4.1), which collectively provide the foundation for analyzing EET in the Kin4B8-carotenoid complexes. In these systems, photoexcitation initially populates the carotenoid S_2 state, and the excitation energy is subsequently transferred to the retinal S_1 excited singlet state (Fig. 6a), a pathway that has been proposed based on spectroscopic observations.[18,26] Extensive experimental (*e.g.*, femtosecond transient absorption and two-dimensional electronic spectroscopy -2DES- measurements) and computational evidence, primarily from xanthorhodopsin complexes containing salinixanthin, supports a dominant Car $S_2 \rightarrow$ *r*PSB S_1 EET pathway, with Car internal conversion from the S_2 state largely suppressed when energy transfer is active.[8–11,13]

We calculated the associated transfer rates using Förster-type energy transfer theory,[31,83,84] as detailed in Section S4.4. This approach is appropriate for the downhill-transfer regime, where excitonic coupling is moderate and energy flow proceeds incoherently. Rates were derived from QM/MMPol calculations of site energies, excitonic couplings, and spectral densities across representative structures, and used to propagate excited-state populations within a kinetic model, implemented in the pyQME software package.[80,81] For each snapshot, the retinal population dynamics were fit to a monoexponential function to extract a characteristic transfer time. Averaging over all trajectories yielded EET times (τ_{EET}) of 59 fs for Kin4B8-ZEA and 60 fs for Kin4B8-LUT (pose A) (Fig. 6c and d). These fall within the ultrafast regime observed in other carotenoid–rhodopsin systems, including the xanthorhodopsin-salinixanthin[8] complex from *Salinibacter ruber* and Gloeobacter rhodopsin (GR), a proton pump from the cyanobacterium *Gloeobacter violaceus*.[23]

To compare with experiment, we estimated the effective EET time from reported excited-state lifetimes. Specifically, Chazan *et al.*[18] reported that the carotenoid S_2 excited-state lifetime is 140 fs (τ_D) when energy transfer is not possible, such as in the Kin4B8-Car complex with a reduced *r*PSB bond. In contrast, when energy transfer occurs, *i.e.*, in the native Kin4B8-LUT complex, the S_2 lifetime is shortened to 60 fs (τ_{DA}). This reduction in lifetime indicates the presence of EET from the carotenoid to the retinal. Based on these lifetimes, the EET time can be estimated as:

$$\tau_{EET}^{exp} = \left(\frac{1}{\tau_{DA}} - \frac{1}{\tau_D}\right)^{-1} \approx 105 \text{ fs} \quad (2)$$

This experimentally inferred value is in good agreement with our simulated results, supporting the validity of our model.

We also estimated the energy transfer efficiency from our computed τ_{EET} using the relation:

$$\Phi = \frac{\tau_D}{\tau_{EET} + \tau_D} \quad (3)$$

We point out that, in our simulations, carotenoid internal relaxation pathways are not explicitly modeled. Therefore, the calculated EET efficiency is determined solely by the computed energy transfer time, τ_{EET}, with the experimental τ_D used as input. We obtain efficiencies of 70.5% for both ZEA and LUT (Fig. 6b and Table S3), modestly higher than the 57% efficiency derived from experiment.[18] This difference likely reflects the slightly faster EET times predicted by our simulations.

Interestingly, the Kin4B8-LUT complex displays a bimodal distribution of EET efficiencies (Fig. 6b), reflecting conformational heterogeneity in the orientation of the carotenoid β-ring within the protein fenestration. In contrast, Kin4B8-ZEA adopts a more stable geometry, leading to narrower distributions of EET times and efficiencies.

To explore the sensitivity of EET dynamics to the excitonic coupling, we recomputed the kinetic model using a range of fixed coupling values (0–275 cm^{-1}), while keeping all other parameters unchanged. For each coupling strength, the EET time and efficiency were calculated across the full ensemble of MD-derived structures, using the original frame-specific site energies. As shown in Fig. S12, the EET time decreases nearly exponentially with increasing coupling, revealing a clear and consistent relationship between coupling magnitude and transfer kinetics.

Among the values tested, a fixed coupling strength of 200 cm^{-1}, which falls within the experimentally estimated range for salinixanthin $S_2 \rightarrow$ *r*PSB S_1 in xanthorhodopsin (160–210 cm^{-1}),[9] yields an EET time of 104 fs and an efficiency of

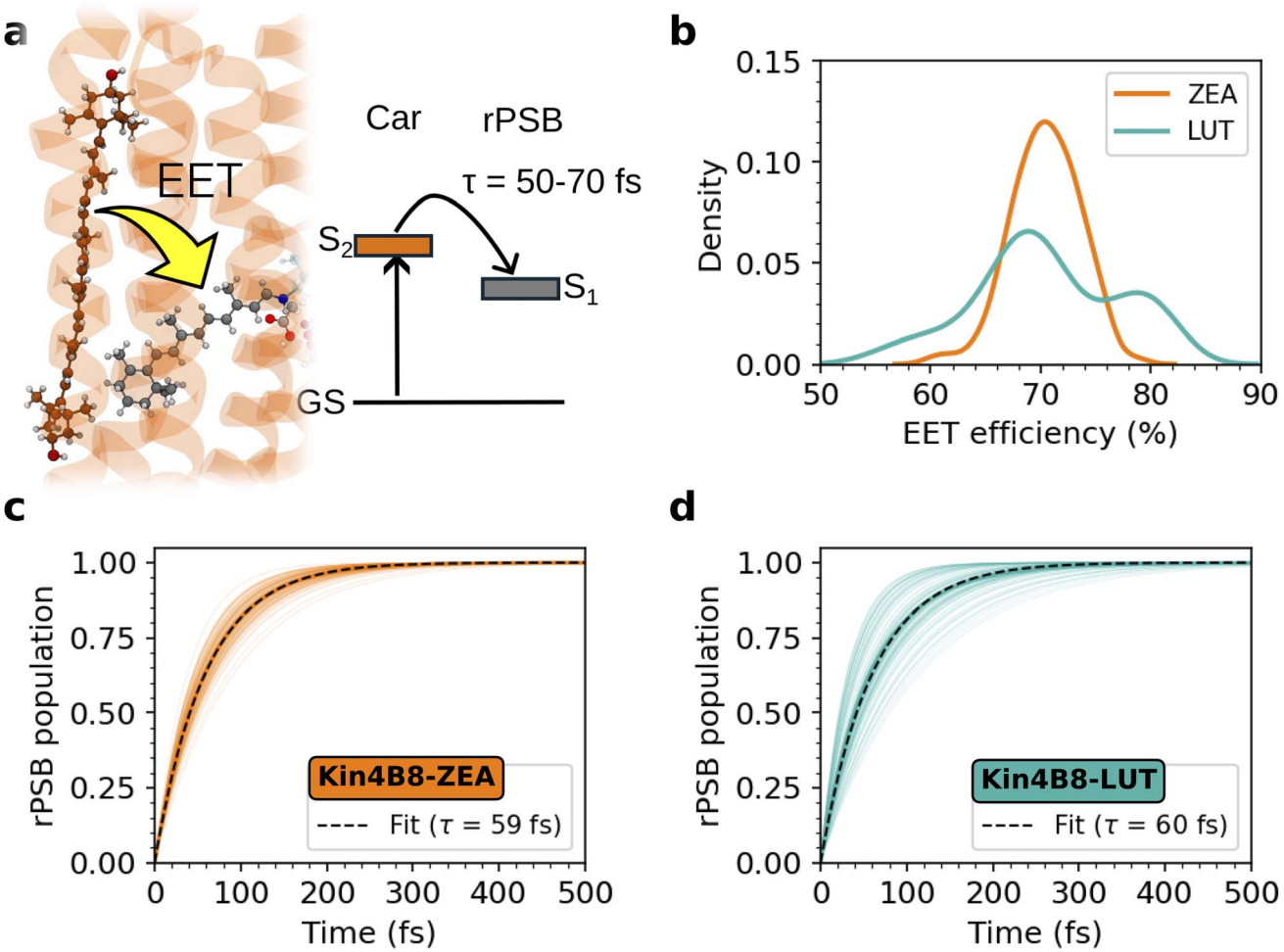

Fig. 6 (a) Schematic representation of the carotenoid-to-retinal energy transfer mechanism. (b) Distribution of energy transfer efficiency along the molecular dynamics simulations. (c and d) Dynamics of the retinal population after transfer from (c) zeaxanthin and (d) lutein. Each thin line represents a snapshot of the MD simulation. The dashed black line represents a fit obtained using a monoexponential function, and the characteristic times are indicated in the legends. The zeaxanthin-rhodopsin represent the protonation state pMS-1, while the results for pMS-2 are shown in Fig. S11.

57%, closely matching experimental observations. This agreement, achieved without adjusting any other parameters, highlights the internal consistency and predictive reliability of our multiscale approach.

Although our simulations yielded an average coupling of 270–280 cm^{-1}, the deviation of 70–80 cm^{-1} is well within the expected uncertainty of our protocol (see Table S4). This is reasonable given the dynamic nature of the system, where fluctuations in the interchromophore distance during the trajectory can significantly affect the excitonic coupling (see Fig. S5).

In summary, our simulations indicate that xanthophylls such as zeaxanthin and lutein can mediate ultrafast and efficient energy transfer to retinal in the Kin4B8 proton pump. Sub-100 fs transfer is enabled by strong excitonic coupling and vibronic overlap, shaped by the protein's fenestration architecture. Notably, this efficiency is achieved without a 4-keto group, a feature traditionally considered important for EET in xanthorhodopsin. In Kin4B8, however, 4-keto carotenoids such as salinixanthin and canthaxanthin do bind to the protein, as confirmed by absorption and circular dichroism spectroscopy,[18,26] yet exhibit poor or no energy transfer. Conversely, nostoxanthin, a hydroxylated carotenoid structurally similar to zeaxanthin, binds effectively and supports EET efficiencies comparable to ZEA.

A comprehensive mutational and screening study involving twelve carotenoids[26] showed that neither 4-keto nor hydroxyl functionalities alone are sufficient to enable EET. Several 4-keto (*e.g.*, salinixanthin, canthaxanthin) and dihydroxy (*e.g.*, astaxanthin reduced) carotenoids bind poorly or not at all, or fail to transfer energy despite binding. Only a small subset, including zeaxanthin, lutein, and nostoxanthin, exhibit both strong binding and high EET efficiency. These carotenoids share not only appropriate polar functional groups but also geometric features compatible with the protein's fenestration, enabling dual hydrogen bonding and optimal chromophore alignment. Our simulations confirm that such anchoring interactions, particularly with Ser208 and Tyr209, are critical for positioning

the carotenoid β-ring at short distances from retinal, a prerequisite for strong excitonic coupling.

Together, these experimental and computational findings reinforce a model in which the protein environment, particularly the geometry and polarity of the fenestration site, plays a dominant role in enabling efficient energy transfer. This represents a shift from earlier models of xanthorhodopsin, where the presence of a 4-keto group was considered essential for energy transfer.[7] Recent screening data from Das *et al.*[26] demonstrated that neither 4-keto nor hydroxyl groups alone predict EET efficiency, highlighting instead the importance of chromophore geometry and protein complementarity. Our results mechanistically confirm this view: we show that carotenoids capable of forming dual hydrogen bonds with Ser208 and Tyr209, and achieving close spatial alignment with retinal, enable strong excitonic coupling independent of specific chemical functionality. This highlights the adaptability of microbial rhodopsins in tuning their photophysical properties through precise protein-ligand complementarity rather than reliance on a specific carotenoid motif.

3 Conclusions

This study provides a molecular-level mechanistic explanation for how hydroxylated carotenoids, such as zeaxanthin and lutein, can mediate efficient light harvesting in microbial rhodopsins despite lacking the canonical 4-keto group previously considered essential for excitation energy transfer.

Using a multiscale computational approach integrating microsecond-scale molecular dynamics, polarizable QM/MM calculations, and excitonic modeling, we show that EET efficiency in Kin4B8-carotenoid complexes arises not from specific functional group chemistry, but from precise protein–ligand geometry. The carotenoid β-ring is anchored by a cooperative hydrogen-bonding network with Ser208 and Tyr209, a configuration stabilized within a conserved protein cavity. This architecture preorganizes the donor(Car)–acceptor(*r*PSB) pair for strong excitonic coupling and sub-100 fs energy transfer.

Our results complement and extend recent experimental work by Das *et al.*,[26] who demonstrated the importance of Ser208 and Tyr209 *via* mutagenesis and QM/MM MD simulations. While their study identified these residues as critical for binding and EET, our enhanced sampling and long-timescale classical MD simulations reveal the persistence and flexibility of the anchoring network over microseconds scale. Additionally, our simulations of the G153F mutant recapitulate the experimentally observed loss of carotenoid binding and EET,[18] confirming the structural necessity of this cavity for carotenoid retention.

We also reproduce experimental absorption and circular dichroism spectra by modeling vibronic lineshapes using spectral densities computed from QM/MM normal-mode analysis. A Förster-type kinetic model, built from QM/MM-derived site energies and excitonic couplings computed with polarizable embedding, predicts energy transfer times below 100 fs and EET efficiencies exceeding 70%, closely matching experimental values. Notably, our analysis identifies the spectral offset between the CD minimum and absorption maximum peaks (in the retinal region) as a potential spectroscopic marker of strong carotenoid–retinal coupling.

Together, these findings support a revised view of carotenoid-assisted phototrophy: rather than relying on specific chemical motifs like keto or hydroxyl groups, rhodopsins tune EET efficiency through protein-guided spatial arrangement and polarity in the fenestration. This conceptual shift is supported by recent screening results,[26] which showed that neither 4-keto nor dihydroxy substitutions alone predict function. Our simulations mechanistically confirm that only carotenoids capable of dual hydrogen bonding and tight retinal alignment enable high-efficiency energy transfer in Kin4B8.

While our study focuses on Kin4B8, the underlying mechanism, *i.e.*, protein-guided chromophore alignment through hydrogen bonding and cavity geometry, is likely relevant to other microbial rhodopsins that bind hydroxylated carotenoids, even when the fenestration architecture differs in detail. The design principles identified here thus provide a transferable framework for understanding excitation energy transfer in diverse rhodopsin proteins and for engineering photoresponsive proteins with tunable optical properties.

As the diversity of microbial rhodopsins binding carotenoids continues to expand,[19,24,25] our multiscale modeling offers a robust strategy for connecting structure to function in natural and synthetic light-harvesting systems. Looking ahead, this framework may also be adapted to explore alternative chromophore arrangements, including retinal–retinal coupling in bistable rhodopsin dimers,[85] where precise geometric control is likewise expected to tune photophysical behavior.

Finally, we acknowledge that polarization effects may also influence the optimized geometries used in this study, particularly since the *r*PSB carries a positive charge and both chromophores engage in hydrogen-bonding interactions with the surrounding protein environment. While polarization was included in the excited-state calculations, incorporating it during QM/MM geometry optimizations could further improve the structural accuracy relevant to excitation energies.[51] However, such methods remain computationally demanding and were beyond the scope of this work. We plan to investigate this aspect in future studies, building on recently developed polarizable QM/MM optimization methodologies.[86,87]

Author contributions

G. S. performed the molecular dynamics and molecular docking simulations. G. S., A. S., and L. P.-G. conducted the protonation state assignments and structural analyses. A. S., C. J., and L. P.-G. carried out the QM/MM(Pol) calculations. C. J. performed the spectral density calculations. L. P.-G. computed the EET couplings. P. M. S. developed the software for the spectroscopy simulations and kinetic model of energy transfer. P. M. S. and L. P.-G. applied the excitonic model and performed the spectroscopy simulations and EET analyses. L. P.-G. conceived the project, supervised the research, and secured funding for computational resources. G. S., P. M. S., and L. P.-G. prepared

the initial draft of the manuscript. All authors contributed to editing and approved the final version of the manuscript.

Conflicts of interest

There are no conflicts to declare.

Data availability

The data supporting this study are available within the manuscript and the SI. Additional data are available from the corresponding author upon reasonable request.

Supplementary information: Details on the selection of the protein protonation microstate and spectroscopic characterization of the *r*PSB site; structural analysis of xanthophyll binding modes in Kin4B8; theoretical background on the exciton Hamiltonian (site energies and electronic couplings), coupling to vibrations, spectroscopy simulations, and kinetic modeling of energy transfer; full computational protocols including molecular docking, classical MD, QM/MM(Pol) DFT calculations, and spectral density calculation. Supplementary tables, figures, and complete references are also provided. See DOI: **https://doi.org/10.1039/d5sc04961j**.

Acknowledgements

The authors thank Prof. Lorenzo Cupellini for insightful discussions and valuable support with the simulation and interpretation of excitonic CD spectra. We are also grateful to Prof. Benedetta Mennucci for helpful scientific discussions. We acknowledge ISCRA for awarding this project access to the LEONARDO supercomputer,[88] owned by the EuroHPC Joint Undertaking, hosted by CINECA (Italy).

References

1 G. D. Scholes, G. R. Fleming, A. Olaya-Castro and R. van Grondelle, Lessons from Nature About Solar Light Harvesting, *Nat. Chem.*, 2011, **3**, 763–774.
2 O. P. Ernst, D. T. Lodowski, M. Elstner, P. Hegemann, L. S. Brown and H. Kandori, Microbial and Animal Rhodopsins: Structures, Functions, and Molecular Mechanisms, *Chem. Rev.*, 2014, **114**, 126–163.
3 E. G. Govorunova, O. A. Sineshchekov, H. Li and J. L. Spudich, Microbial Rhodopsins: Diversity, Mechanisms, and Optogenetic Applications, *Annu. Rev. Biochem.*, 2017, **86**, 845–872.
4 H. Kandori, Retinal Proteins: Photochemistry and Optogenetics, *Bull. Chem. Soc. Jpn.*, 2020, **93**, 76–85.
5 A. Rozenberg, K. Inoue, H. Kandori and O. Béjà, Microbial Rhodopsins: The Last Two Decades, *Annu. Rev. Microbiol.*, 2021, **75**, 427–447.
6 K. Inoue, Photochemistry of the retinal chromophore in microbial rhodopsins, *J. Phys. Chem. B*, 2023, **127**, 9215–9222.
7 S. P. Balashov, E. S. Imasheva, V. A. Boichenko, J. Antón, J. M. Wang and J. K. Lanyi, Xanthorhodopsin: A Proton Pump with a Light-Harvesting Carotenoid Antenna, *Science*, 2005, **309**, 2061–2064.
8 S. P. Balashov, E. S. Imasheva, J. M. Wang and J. K. Lanyi, Excitation Energy-Transfer and the Relative Orientation of Retinal and Carotenoid in Xanthorhodopsin, *Biophys. J.*, 2008, **95**, 2402–2414.
9 T. Polívka, S. P. Balashov, P. Chábera, E. S. Imasheva, A. Yartsev, V. Sundström and J. K. Lanyi, Femtosecond Carotenoid to Retinal Energy Transfer in Xanthorhodopsin, *Biophys. J.*, 2009, **96**, 2268–2277.
10 J. Zhu, I. Gdor, E. Smolensky, N. Friedman, M. Sheves and S. Ruhman, Photoselective ultrafast investigation of xanthorhodopsin and its carotenoid antenna salinixanthin, *J. Phys. Chem. B*, 2010, **114**, 3038–3045.
11 I. Gdor, J. Zhu, B. Loevsky, E. Smolensky, N. Friedman, M. Sheves and S. Ruhman, Investigating excited state dynamics of salinixanthin and xanthorhodopsin in the near-infrared, *Phys. Chem. Chem. Phys.*, 2011, **13**, 3782–3787.
12 V. A. Anashkin, Y. V. Bertsova, A. M. Mamedov, M. D. Mamedov, A. M. Arutyunyan, A. A. Baykov and A. V. Bogachev, Engineering a carotenoid-binding site in Dokdonia sp. PRO95 Na^+-translocating rhodopsin by a single amino acid substitution, *Photosynth. Res.*, 2018, **136**, 161–169.
13 F. Segatta, I. Gdor, J. Réhault, S. Taioli, N. Friedman, M. Sheves, I. Rivalta, S. Ruhman, G. Cerullo and M. Garavelli, Ultrafast Carotenoid to Retinal Energy Transfer in Xanthorhodopsin Revealed by the Combination of Transient Absorption and Two-Dimensional Electronic Spectroscopy, *Chem.–Eur. J.*, 2018, **24**, 12084–12092.
14 K. Chuon, J.-g. Shim, S.-H. Kim, S.-G. Cho, S. Meas, K.-W. Kang, J.-H. Kim, I. Das, M. Sheves and K.-H. Jung, The Role of Carotenoids in Proton-Pumping Rhodopsin as a Primitive Solar Energy Conversion System, *J. Photochem. Photobiol., B*, 2021, **221**, 112241.
15 K. Chuon, J.-g. Shim, K.-W. Kang, S.-G. Cho, C. Hour, S. Meas, J.-H. Kim, A. Choi and K.-H. Jung, Carotenoid Binding in Gloeobacteria Rhodopsin Provides Insights into Divergent Evolution of Xanthorhodopsin Types, *Commun. Biol.*, 2022, **5**, 512.
16 K. Kopejtka, J. Tomasch, D. Kaftan, A. T. Gardiner, D. Bína, Z. Gardian, C. Bellas, A. Dröge, R. Geffers, R. Sommaruga, *et al.*, A bacterium from a mountain lake harvests light using both proton-pumping xanthorhodopsins and bacteriochlorophyll-based photosystems, *Proc. Natl. Acad. Sci. U. S. A*, 2022, **119**, e2211018119.
17 M. Ghosh, R. Misra, S. Bhattacharya, K. Majhi, K.-H. Jung and M. Sheves, Retinal–Carotenoid Interactions in a Sodium-Ion-Pumping Rhodopsin: Implications on Oligomerization and Thermal Stability, *J. Phys. Chem. B*, 2023, **127**, 2128–2137.
18 A. Chazan, I. Das, T. Fujiwara, S. Murakoshi, A. Rozenberg, A. Molina-Márquez, F. K. Sano, T. Tanaka, P. Gómez-Villegas, S. Larom, *et al.*, Phototrophy by Antenna-Containing Rhodopsin Pumps in Aquatic Environments, *Nature*, 2023, **615**, 535–540.

19 T. Fujiwara, T. Hosaka, M. Hasegawa-Takano, Y. Nishimura, K. Tominaga, K. Mori, S. Nishino, Y. Takahashi, T. Uchikubo-Kamo, K. Hanada, *et al.*, Carotenoids bind rhodopsins and act as photocycle-accelerating pigments in marine *Bacteroidota*, *Nat. Microbiol.*, 2025, DOI: 10.1038/s41564-025-02109-1.
20 L. E. Petrovskaya, V. A. Bolshakov, E. P. Lukashev, E. A. Kryukova, E. G. Maksimov, A. B. Rubin, D. A. Dolgikh, S. P. Balashov and M. P. Kirpichnikov, Engineering of Thermal Stability in the Recombinant Xanthorhodopsin from Salinibacter ruber, *Biochim. Biophys. Acta Bioenerg.*, 2025, **1866**(2), 149547.
21 E. S. Imasheva, S. P. Balashov, A. R. Choi, K.-H. Jung and J. K. Lanyi, Reconstitution of Gloeobacter violaceus Rhodopsin with a Light-Harvesting Carotenoid Antenna, *Biochemistry*, 2009, **48**, 10948–10955.
22 S. P. Balashov, E. S. Imasheva, A. R. Choi, K.-H. Jung, S. Liaaen-Jensen and J. K. Lanyi, Reconstitution of Gloeobacter Rhodopsin with Echinenone: Role of the 4-Keto Group, *Biochemistry*, 2010, **49**, 9792–9799.
23 E. S. S. Iyer, I. Gdor, T. Eliash, M. Sheves and S. Ruhman, Efficient Femtosecond Energy Transfer from Carotenoid to Retinal in Gloeobacter Rhodopsin–Salinixanthin Complex, *J. Phys. Chem. B*, 2015, **119**, 2345–2349.
24 G. Tzlil, M. d. C. Marín, Y. Matsuzaki, P. Nag, S. Itakura, Y. Mizuno, S. Murakoshi, T. Tanaka, S. Larom, M. Konno, *et al.*, Structural Insights into Light Harvesting by Antenna-Containing Rhodopsins in Marine Asgard Archaea, *Nat. Microbiol.*, 2025, **10**, 1484–1500.
25 M. d. C. Marín Pérez, S. Murakoshi, A. Rozenberg, T. Tanaka, M. Konno, W. Shihoya, O. Nureki, K. Inoue and O. Béjà, Light-harvesting by antenna-containing xanthorhodopsin from an Antarctic cyanobacterium, *bioRxiv*, 2025, DOI: 10.1101/2025.06.10.658827.
26 I. Das, A. Chazan, J. R. Church, S. Larom, R. León, P. Gómez-Villegas, D. Bárcenas-Pérez, J. Cheel, M. Koblížek, O. Béjà, I. Schapiro and M. Sheves, Selective Choice of the Efficient Carotenoid Antenna by a Xanthorhodopsin: Controlling Factors for Binding and Excitation Energy Transfer, *JACS Au*, 2025, **5**(7), 3070–3081.
27 W. Humphrey, A. Dalke and K. Schulten, VMD—Visual Molecular Dynamics, *J. Mol. Graph.*, 1996, **14**, 33–38.
28 H. Fidder, J. Knoester and D. A. Wiersma, Optical Properties of Disordered Molecular Aggregates: A Numerical Study, *J. Chem. Phys.*, 1991, **95**, 7880–7890.
29 C. Curutchet, A. Muñoz-Losa, S. Monti, J. Kongsted, G. D. Scholes and B. Mennucci, Electronic Energy Transfer in Condensed Phase Studied by a Polarizable QM/MM Model, *J. Chem. Theory Comput.*, 2009, **5**, 1838–1848.
30 C. Curutchet and B. Mennucci, Quantum chemical studies of light harvesting, *Chem. Rev.*, 2017, **117**, 294–343.
31 L. Cupellini, M. Corbella, B. Mennucci and C. Curutchet, Electronic Energy Transfer in Biomacromolecules, *Wiley Interdiscip. Rev.: Comput. Mol. Sci.*, 2019, **9**, e1392.
32 A. K. Dioumaev, J. M. Wang, Z. Bálint, G. Váró and J. K. Lanyi, Proton transport by Proteorhodopsin requires that the Retinal Schiff Base counterion Asp-97 be anionic, *Biochemistry*, 2003, **42**, 6582–6587.
33 A. Altun, S. Yokoyama and K. Morokuma, Spectral tuning in visual pigments: an ONIOM (QM: MM) study on bovine rhodopsin and its mutants, *J. Phys. Chem. B*, 2008, **112**, 6814–6827.
34 G. Tomasello, G. Olaso-Gonzalez, P. Altoe, M. Stenta, L. Serrano-Andres, M. Merchan, G. Orlandi, A. Bottoni and M. Garavelli, Electrostatic control of the photoisomerization efficiency and optical properties in visual pigments: on the role of counterion quenching, *J. Am. Chem. Soc.*, 2009, **131**, 5172–5186.
35 L. Pedraza-González, L. De Vico, M. d. C. Marín, F. Fanelli and M. Olivucci, a-ARM: Automatic Rhodopsin Modeling with Chromophore Cavity Generation, Ionization State Selection and External Counter-ion Placement, *J. Chem. Theory Comput.*, 2019, **15**, 3134–3152.
36 Y. Nakajima, L. Pedraza-González, L. Barneschi, K. Inoue, M. Olivucci and H. Kandori, Pro219 is an Electrostatic Color Determinant in the Light-Driven Sodium Pump KR2, *Commun. Biol.*, 2021, **4**, 1185.
37 M. Broser, A. Spreen, P. E. Konold, E. Schiewer, S. Adam, V. Borin, I. Schapiro, R. Seifert, J. T. M. Kennis, Y. A. Bernal Sierra, *et al.*, NeoR, a Near-Infrared Absorbing Rhodopsin, *Nat. Commun.*, 2020, **11**, 5682.
38 P. Malakar, S. Gholami, M. Aarabi, I. Rivalta, M. Sheves, M. Garavelli and S. Ruhman, Retinal Photoisomerization Versus Counterion Protonation in Light- and Dark-Adapted Bacteriorhodopsin and Its Primary Photoproduct, *Nat. Commun.*, 2024, **15**, 2136.
39 R. Palombo, L. Barneschi, L. Pedraza-González, X. Yang and M. Olivucci, Picosecond quantum-classical dynamics reveals that the coexistence of light-induced microbial and animal chromophore rotary motion modulates the isomerization quantum yield of heliorhodopsin, *Phys. Chem. Chem. Phys.*, 2024, **26**, 10343–10356.
40 J. R. Church, P. Nag, T. Dogon and I. Schapiro, Origin of the red-shifted absorption maximum in channelrhodopsin Chrimson, *Chem. Commun.*, 2025, **61**, 13117–13120.
41 L. Pedraza-González, L. Barneschi, M. Marszałek, D. Padula, L. De Vico and M. Olivucci, Automated QM/MM Screening of Rhodopsin Variants with Enhanced Fluorescence, *J. Chem. Theory Comput.*, 2023, **19**(1), 293–310.
42 S. Jurinovich, L. Cupellini, C. A. Guido and B. Mennucci, EXAT: EXcitonic Analysis Tool, *J. Comput. Chem.*, 2018, **39**, 279–286.
43 T. Yanai, D. P. Tew and N. C. Handy, A new hybrid exchange–correlation functional using the Coulomb-attenuating method (CAM-B3LYP), *Chem. Phys. Lett.*, 2004, **393**, 51–57.
44 P. C. Hariharan and J. A. Pople, The influence of polarization functions on molecular orbital hydrogenation energies, *Theor. Chim. Acta*, 1973, **28**, 213–222.
45 I. V. Rostov, R. D. Amos, R. Kobayashi, G. Scalmani and M. J. Frisch, Studies of the ground and excited-state surfaces of the retinal chromophore using CAM-B3LYP, *J. Phys. Chem. B*, 2010, **114**, 5547–5555.

46 D. Kröner and J. P. Götze, Modeling of a violaxanthin–chlorophyll b chromophore pair in its LHCII environment using CAM-B3LYP, *J. Photochem. Photobiol., B*, 2012, **109**, 12–19.
47 G. Pescitelli and R. W. Woody, The Exciton Origin of the Visible Circular Dichroism Spectrum of Bacteriorhodopsin, *J. Phys. Chem. B*, 2012, **116**, 6751–6763.
48 S. Knecht, C. M. Marian, J. Kongsted and B. Mennucci, On the photophysics of carotenoids: a multireference DFT study of peridinin, *J. Phys. Chem. B*, 2013, **117**, 13808–13815.
49 J. P. Götze and W. Thiel, TD-DFT and DFT/MRCI study of electronic excitations in Violaxanthin and Zeaxanthin, *Chem. Phys.*, 2013, **415**, 247–255.
50 J. P. Götze, D. Kröner, S. Banerjee, B. Karasulu and W. Thiel, Carotenoids as a Shortcut for Chlorophyll Soret-to-Q Band Energy Flow, *Chem Phys Chem*, 2014, **15**, 3392–3401.
51 S. Caprasecca, S. Jurinovich, L. Viani, C. Curutchet and B. Mennucci, Geometry optimization in polarizable QM/MM models: the induced dipole formulation, *J. Chem. Theory Comput.*, 2014, **10**, 1588–1598.
52 J. P. Goötze, Vibrational relaxation in carotenoids as an explanation for their rapid optical properties, *J. Phys. Chem. B*, 2019, **123**, 2203–2209.
53 M. J. Frisch, G. W. Trucks, H. B. Schlegel, G. E. Scuseria, M. A. Robb, J. R. Cheeseman, G. Scalmani, V. Barone, G. A. Petersson, H. Nakatsuji, X. Li, M. Caricato, A. V. Marenich, J. Bloino, B. G. Janesko, R. Gomperts, B. Mennucci, H. P. Hratchian, J. V. Ortiz, A. F. Izmaylov, J. L. Sonnenberg, D. Williams-Young, F. Ding, F. Lipparini, F. Egidi, J. Goings, B. Peng, A. Petrone, T. Henderson, D. Ranasinghe, V. G. Zakrzewski, J. Gao, N. Rega, G. Zheng, W. Liang, M. Hada, M. Ehara, K. Toyota, R. Fukuda, J. Hasegawa, M. Ishida, T. Nakajima, Y. Honda, O. Kitao, H. Nakai, T. Vreven, K. Throssell, J. A. Montgomery Jr, J. E. Peralta, F. Ogliaro, M. J. Bearpark, J. J. Heyd, E. N. Brothers, K. N. Kudin, V. N. Staroverov, T. A. Keith, R. Kobayashi, J. Normand, K. Raghavachari, A. P. Rendell, J. C. Burant, S. S. Iyengar, J. Tomasi, M. Cossi, J. M. Millam, M. Klene, C. Adamo, R. Cammi, J. W. Ochterski, R. L. Martin, K. Morokuma, O. Farkas, J. B. Foresman and D. J. Fox, *Gaussian 16 Revision A.03*, Gaussian Inc, Wallingford CT, 2016.
54 D. Loco and L. Cupellini, Modeling the Absorption Lineshape of Embedded Systems from Molecular Dynamics: A Tutorial Review, *Int. J. Quantum Chem.*, 2019, **119**, e25726.
55 C. John, L. Pedraza-González, E. Betti, L. Cupellini and B. Mennucci, A Computational Approach to Modeling Excitation Energy Transfer and Quenching in Light-Harvesting Complexes, *J. Phys. Chem. B*, 2024, **129**, 117–127.
56 M. E. Casida and D. R. Salahub, Asymptotic correction approach to improving approximate exchange–correlation potentials: Time-dependent density-functional theory calculations of molecular excitation spectra, *J. Chem. Phys.*, 2000, **113**, 8918–8935.
57 S. Corni, R. Cammi, B. Mennucci and J. Tomasi, Electronic excitation energies of molecules in solution within continuum solvation models: Investigating the discrepancy between state-specific and linear-response methods, *J. Chem. Phys.*, 2005, **123**, 134512.
58 D. Loco, L. Lagardère, O. Adjoua and J.-P. Piquemal, Atomistic Polarizable Embeddings: Energy, Dynamics, Spectroscopy, and Reactivity, *Acc. Chem. Res.*, 2021, **54**, 2812–2822.
59 F. Lipparini, General Linear Scaling Implementation of Polarizable Embedding Schemes, *J. Chem. Theory Comput.*, 2019, **15**, 4312–4317.
60 M. Bondanza, M. Nottoli, L. Cupellini, F. Lipparini and B. Mennucci, Polarizable Embedding QM/MM: The Future Gold Standard for Complex (Bio)Systems?, *Phys. Chem. Chem. Phys.*, 2020, **22**, 14433–14448.
61 C. A. Guido, A. Chrayteh, G. Scalmani, B. Mennucci and D. Jacquemin, Simple protocol for capturing both linear-response and state-specific effects in excited-state calculations with continuum solvation models, *J. Chem. Theory Comput.*, 2021, **17**, 5155–5164.
62 M. Nottoli, M. Bondanza, P. Mazzeo, L. Cupellini, C. Curutchet, D. Loco, L. Lagardère, J.-P. Piquemal, B. Mennucci and F. Lipparini, QM/AMOEBA Description of Properties and Dynamics of Embedded Molecules, *Wiley Interdiscip. Rev.: Comput. Mol. Sci.*, 2023, **13**, e1674.
63 D. Di Prima, L. Pedraza-González, P. Reinholdt, J. Kongsted and B. Mennucci, Fluorescent Rhodopsins: A Challenging Test for Cost-Effective QM/MM Approaches, *J. Phys. Chem. A*, 2025, **129**(6), 1769–1778.
64 S. R. Marder, C. B. Gorman, B. G. Tiemann, J. W. Perry, G. Bourhill and K. Mansour, Relation between bond-length alternation and second electronic hyperpolarizability of conjugated organic molecules, *Science*, 1993, **261**, 186–189.
65 S. R. Marder, L.-T. Cheng, B. G. Tiemann, A. C. Friedli, M. Blanchard-Desce, J. W. Perry and J. Skindhøj, Large first hyperpolarizabilities in push-pull polyenes by tuning of the bond length alternation and aromaticity, *Science*, 1994, **263**, 511–514.
66 G. G. Kochendoerfer, S. W. Lin, T. P. Sakmar and R. A. Mathies, How color visual pigments are tuned, *Trends Biochem. Sci.*, 1999, **24**, 300–305.
67 J. P. Götze, Atomistic modeling of large biological systems and the need for (un-)realistic approaches, *Chem. Model*, 2024, **18**, 76–101.
68 P. B. Coto, A. Strambi, N. Ferré and M. Olivucci, The color of rhodopsins at the ab initio multiconfigurational perturbation theory resolution, *Proc. Natl. Acad. Sci. U. S. A*, 2006, **103**, 17154–17159.
69 K. Fujimoto, S. Hayashi, J.-y. Hasegawa and H. Nakatsuji, Theoretical studies on the color-tuning mechanism in retinal proteins, *J. Chem. Theory Comput.*, 2007, **3**, 605–618.
70 K. Fujimoto, J.-y. Hasegawa and H. Nakatsuji, Color tuning mechanism of human red, green, and blue cone pigments: SAC-CI theoretical study, *Bull. Chem. Soc. Jpn.*, 2009, **82**, 1140–1148.
71 H. L. Luk, N. Bhattacharyya, F. Montisci, J. M. Morrow, F. Melaccio, A. Wada, M. Sheves, F. Fanelli, B. S. Chang and M. Olivucci, Modulation of thermal noise and spectral

sensitivity in Lake Baikal cottoid fish rhodopsins, *Sci. Rep.*, 2016, **6**, 38425.

72 K. Inoue, M. del Carmen Marín, S. Tomida, R. Nakamura, Y. Nakajima, M. Olivucci and H. Kandori, Red-shifting mutation of light-driven sodium-pump rhodopsin, *Nat. Commun.*, 2019, **10**, 1993.

73 L. Barneschi, E. Marsili, L. Pedraza-González, D. Padula, L. De Vico, D. Kaliakin, A. Blanco-González, N. Ferré, M. Huix-Rotllant, M. Filatov and M. Olivucci, On the fluorescence enhancement of arch neuronal optogenetic reporters, *Nat. Commun.*, 2022, **13**, 6432.

74 D. Wijayaratna, F. Sacchetta, L. Pedraza-González, F. Fanelli, T. Sugihara, M. Koyanagi, S. Piyawardana, K. Ghotra, W. Thotamune, A. Terakita, *et al.*, In-silico predicted mouse melanopsins with blue spectral shifts deliver efficient subcellular signaling, *Cell Commun. Signal.*, 2024, **22**, 394.

75 K. J. Fujimoto and S. P. Balashov, Vibronic Coupling Effect on Circular Dichroism Spectrum: Carotenoid–Retinal Interaction in Xanthorhodopsin, *J. Chem. Phys.*, 2017, **146**, 0951011–09510110.

76 H. Luecke, B. Schobert, J. Stagno, E. S. Imasheva, J. M. Wang, S. P. Balashov and J. K. Lanyi, Crystallographic Structure of Xanthorhodopsin, the Light-Driven Proton Pump with a Dual Chromophore, *Proc. Natl. Acad. Sci. U. S. A*, 2008, **105**, 16561–16565.

77 B. P. Krueger, G. D. Scholes and G. R. Fleming, Calculation of Couplings and Energy-Transfer Pathways Between the Pigments of LH2 by the Ab Initio Transition Density Cube Method, *J. Phys. Chem. B*, 1998, **102**, 5378–5386.

78 L. Pedraza-González, E. Cignoni, J. D'Ascenzi, L. Cupellini and B. Mennucci, How the pH Controls Photoprotection in the Light-Harvesting Complex of Mosses, *J. Am. Chem. Soc.*, 2023, **145**, 7482–7494.

79 K. J. Fujimoto, Electronic Couplings and Electrostatic Interactions Behind the Light Absorption of Retinal Proteins, *Front. Mol. Biosci.*, 2021, **8**, 752700.

80 P. Saraceno, V. Sláma and L. Cupellini, First-Principles Simulation of Excitation Energy Transfer and Transient Absorption Spectroscopy in the CP29 Light-Harvesting Complex, *J. Chem. Phys.*, 2023, **159**, 184112.

81 P. Saraceno and L. Cupellini, pyQME: a Package for Open Quantum System Dynamics and Spectroscopies Simulations in the Exciton Framework, 2024, **https://github.com/Molecolab-Pisa/pyQME**.

82 S. Jana, K.-H. Jung and M. Sheves, The chirality origin of retinal-carotenoid complex in gloeobacter rhodopsin: a temperature-dependent excitonic coupling, *Sci. Rep.*, 2020, **10**, 13992.

83 G. D. Scholes, X. J. Jordanides and G. R. Fleming, Adapting the Förster Theory of Energy Transfer for Modeling Dynamics in Aggregated Molecular Assemblies, *J. Phys. Chem. B*, 2001, **105**, 1640–1651.

84 I. L. Medintz and N. Hildebrandt, *FRET-Förster resonance energy transfer: from theory to applications*, John Wiley & Sons, 2013.

85 I. H. M. van Stokkum, J. Dostal, T. N. Do, L. Fu, G. Madej, C. Ziegler, P. Hegemann, M. Kloz, M. Broser and J. T. M. Kennis, Retinal to Retinal Energy Transfer in a Bistable Microbial Rhodopsin Dimer, *J. Am. Chem. Soc.*, 2025, **147**, 14468–14480.

86 M. Bondanza, T. Nottoli, M. Nottoli, L. Cupellini, F. Lipparini and B. Mennucci, The OpenMMPol library for polarizable QM/MM calculations of properties and dynamics, *J. Chem. Phys.*, 2024, **160**, 134106.

87 T. Nottoli, M. Bondanza, F. Lipparini and B. Mennucci, A polarizable CASSCF/MM approach using the interface between OpenMMPol library and CFour, *J. Comput. Chem.*, 2025, **46**, e27550.

88 M. Turisini, M. Cestari and G. Amati, LEONARDO: A Pan-European Pre-Exascale Supercomputer for HPC and AI Applications, *JLSRF*, 2024, **9**, 1–26.